OPEN ACCESS

Electrochemical Characterization of Nickel/Gadolinia Doped Ceria Fuel Electrodes under $H_2/H_2O/CO/CO_2$-Atmospheres

To cite this article: D. Esau *et al* 2024 *J. Electrochem. Soc.* **171** 054522

Journal of The Electrochemical Society, 2024 **171** 054522

Electrochemical Characterization of Nickel/Gadolinia Doped Ceria Fuel Electrodes under $H_2/H_2O/CO/CO_2$-Atmospheres

D. Esau,[1,z] C. Grosselindemann,[1] S. P. Sckuhr,[1] F. Kullmann,[1] A. Lindner,[1] Z. Liang,[2] F. M. Fuchs,[3] and A. Weber[1,*]

[1] *Institute for Applied Materials—Electrochemical Technologies (IAM-ET), Karlsruhe Institute of Technology (KIT), Karlsruhe D-76131, Germany*
[2] *Laboratory for Electron Microscopy (LEM) Karlsruhe Institute of Technology (KIT), Karlsruhe D-76131, Germany*
[3] *Kerafol Keramische Folien GmbH & Co. KG, Eschenbach D-92676, Germany*

Modelling of the co-electrolysis process requires understanding of the underlying reaction pathways under $H_2/H_2O/CO/CO_2$-atmospheres. These include the electrochemical steam reduction/hydrogen oxidation, the electrochemical CO_2 reduction/CO oxidation and their coupling via the catalytic (reverse) water gas shift reaction ((R)WGS). The assumption of a very fast RWGS and therefore neglectable electrochemical CO_2 conversion is commonly used to model the co-electrolysis process. In contrast, previous studies on Ni/GDC fuel electrodes suggest that the electrochemical conversion of CO/CO_2 can be present in $H_2/H_2O/CO/CO_2$-atmospheres. To deconvolute surface-related and non-surface-related processes in the impedance response we present results from a complex variation of operating parameters for process identification by the use of electrochemical impedance spectroscopy and the subsequent impedance analysis by the distribution of relaxation times. A physically meaningful equivalent circuit model, based on a single channel transmission line, is then derived. The model enables quantification of the surface reaction resistance under varied C/H-ratios. From a kinetic analysis it is shown that the electrochemical H_2/H_2O conversion is dominant for $y_{CO} + y_{CO_2} \leqslant 50\%$ and electrochemical CO/CO_2-conversion onsets from $y_{CO} + y_{CO_2} \geqslant 60\%$.

 [DOI: 10.1149/1945-7111/ad4c10]

Manuscript submitted February 1, 2024; revised manuscript received May 10, 2024. Published May 29, 2024. *This paper is part of the JES Focus Issue on SOFC XVIII: Advances in Solid Oxide Fuel Cell and Electrolysis Cell Technology.*

List of Symbols

Latin Letters

A_{cell}	geometric cell area (cm^2)
a	exponent describing hydrogen partial pressure dependency of the fuel electrode´s exchange current density (-)
b	exponent describing steam partial pressure dependency of the fuel electrode´s exchange current density (-)
c_{chem}	chemical capacitance ($F\ cm^{-1}$)
D_i	gas diffusion coefficient of the component i ($m^2\ s^{-1}$)
E_a	activation energy ($kJ\ mol^{-1}$)
F	faraday constant ($As\ mol^{-1}$)
G_{eff}	effective gas diffusion parameter (m^{-1})
$\Delta_R H^0$	standard reaction enthalpy ($kJ\ mol^{-1}$)
j_0	exchange current density ($A\ m^{-2}$)
L	electrode thickness (μm)
L_{Diff}	diffusion length (m)
P	overall pressure (atm)
p_i	partial pressure of component i (atm)
R	universal gas constant 8.314 ($J\ mol^{-1}\ K^{-1}$)
R_{Diff}	gas diffusion resistance ($\Omega\ cm^2$)
R_i	area specific resistance contribution i ($\Omega\ cm^2$)
R_0	area specific ohmic resistance ($\Omega\ cm^2$)
r_{ion}	incremental ionic resistance per unit length ($\Omega\ cm^{-1}$)
r_{SR}	surface reaction resistance (Ω cm)
T	temperature (K)
y_i	mole fraction in gas phase of component i (-)
z	number of exchanged electrons (-)
Z	impedance ($\Omega\ cm^2$)

Greek Letters

γ	exponential prefactor ($A\ m^{-2}$)
ε	volume fraction (-)
ζ	incremental charge transfer impedance (Ω cm)
λ	penetration depth (μm)
σ_i	conductivity ($S\ cm^{-1}$)
τ	tortuosity (-)
χ_i	incremental electronic/ionic charge transport impedance ($\Omega\ cm^{-1}$)
Ψ	microstructure parameter (-)
ω	frequency ($rad\ s^{-1}$)

Sub - and superscripts

a	activation
cell	cell
chem	chemical
CO	carbon monoxide
CO_2	carbon dioxide
Diff	gas diffusion
eff	effective
el	electronic
eq820 °C	equlibrium composition of gas mixture at 820 °C
GDC	gadolinia-doped ceria
H_2	hydrogen
H_2O	steam
He	helium
ion	ionic
LF	low frequency
mol	molar
HF	high frequency
N_2	nitrogen
OCV	open-circuit voltage
ox	oxidized species
r	reduced species
SR	surface reaction

*Electrochemical Society Member.
[z]E-mail: daniel.esau@kit.edu

The simultaneous reduction of steam (H_2O) and carbon dioxide (CO_2) in an electrolyzer, widely known as the co-electrolysis process, represents an efficient way to produce tailored mixtures of carbon monoxide (CO) and hydrogen (H_2) (synthesis gas). A reliable prediction of outlet compositions, cell performance and degradation is only possible with a sufficient understanding of the underlying physical processes. In contrast to steam electrolysis, physical processes during co-electrolysis are more complex, mainly due to the higher amount of possible reactions that can occur on the cathode surface. From a macroscopic view, electrochemical reduction of CO_2 as well as of H_2O can occur on the cathode of an ideal co-electrolyzer:

$$CO_2 + 2e^- \rightleftharpoons CO + O^{2-}, \quad [1]$$

$$H_2O + 2e^- \rightleftharpoons H_2 + O^{2-}, \quad [2]$$

while the ratio of both will determine the resulting product stoichiometry. Additionally, nickel containing cathodes have a high catalytic effect on the reverse water gas shift reaction (RWGS):

$$CO_2 + H_2 \rightleftharpoons CO + H_2O,\ \Delta_R H^0 = 41\ \text{kJ mol}^{-1}, \quad [3]$$

which effectively causes a coupling of reactions 1 and 2. The RWGS is often assumed as in equilibrium due to its fast kinetics at temperatures above 800 °C.[1] Also, one may assume that an electrochemical reduction of CO_2 can be completely neglected and any CO_2 conversion is happening via the RWGS. This assumption though, can only be valid up to a certain p_{CO_2}/p_{H_2O} ratio. Kromp et al. have demonstrated the validity of this assumption with a nickel/yttria stabilized zirconia (Ni/YSZ) fuel electrode supported cell at a p_{CO_2}/p_{H_2O} ratio of 1, by comparing effective kinetic parameters of hydrogen-steam-nitrogen operation to ones obtained with a reformate gas mixture.[1] Based on an analysis of impedance measurements and polarization curves at various product compositions Wolf et al. proposed a boundary for the onset of the electrochemical CO_2 reduction on Ni/YSZ fuel electrode supported cells at a steam content of 30%, while above this value the CO_2 reduction predominantly happens via the RWGS.[2]

On the other hand, electrodes with mixed ionic electronic conducting (MIEC) materials like nickel/gadolinia doped ceria (Ni/GDC) can have a different affinity towards the electrochemical CO_2 reduction[3] and thus could show a different boundary for its onset in co-electrolysis conditions. Generally, a meaningful analysis of separate activation resistance contributions of Ni/GDC electrodes can be difficult due to the very different impedance characteristics compared to Ni/YSZ, especially as often a poor separation of gas diffusion and electrode activation in the impedance spectrum is observed.[3–8]

In the first part of this study, results from a comprehensive parameter variation on symmetrical cells with Ni/GDC electrodes are shown to identify characteristic frequency ranges of gas diffusion, surface-reaction, and bulk/interface resistance contributions under $H_2/H_2O/CO/CO_2$-atmospheres. These variations include: a variation of the fuel gas composition, addition of small amounts of H_2S to the gas phase, temperature variation, and a change of inert diluent from nitrogen to helium.

Aided by the knowledge gained from these parameter variations, a well-fitting, physically meaningful equivalent circuit is derived. The circuit contains elements accounting for gas diffusion losses, the surface reaction coupled with charge transport in the porous electrode and interface contributions. To avoid overparameterization, gas diffusion losses as well as the ionic resistance are estimated appropriately. Effective conductivities are calculated with literature data and corrected through quantification of microstructural parameters by focused ion beam—scanning electron microscopy (FIB-SEM) tomography. Fitting with the derived equivalent circuit allows for quantification of the surface reaction resistance. By determining the kinetics of the surface reaction resistance under different C/H ratios, we identify a threshold for a shift from electrochemical H_2/H_2O conversion + (R)WGS towards the onset of the electrochemical CO/CO_2 conversion on Ni/GDC fuel electrodes.

Experimental

Within this contribution, planar symmetrical cells with an active area of 1 cm^2 were analyzed. For electrochemical characterization, Ni/GDC electrodes on a 3 mol% yttria stabilized zirconia (3YSZ) electrolyte were used. The electrodes exhibited an interlayer of GDC between electrolyte and Ni/GDC, as visualized in Fig. 5a. A comparable SEM image as well as the cell configuration is provided in an earlier paper.[6] Standardized reduction procedures are always performed within the startup of every cell.

A Helios G4 FX dual beam system combining scanning electron microscopy (SEM) and gallium focused ion beam (Ga^+-FIB) was employed for milling and imaging to achieve a 3D FIB/SEM reconstruction (voxel size 15 × 15 × 15 nm^3). High phase contrast between GDC, nickel and pore space is enabled by an in-column BSE detector. Image processing and evaluation were performed using the software toolbox GeoDict.[9] For a detailed explanation on how the resulting image slices were processed to yield the volume fraction ε_{GDC} and tortuosity τ_{GDC} values of the GDC phase, we refer to an earlier publication.[10]

Electrochemical measurements were performed in a test rig described in Ref. 11. A total flow rate of 500 sccm is set (250 sccm per electrode), to minimize gas conversion during impedance measurements. Synthetic steam is produced in an external upstream combustion chamber by mixing oxygen to the fuel. CO_2, CO and nitrogen are added after combustion to avoid unwanted CO oxidation and to ensure a well-defined gas mixture at the electrode surface. The gas mixtures were always adjusted so that the mixture reaches the cell in equilibrium. Equilibrium partial pressure calculations were performed with the software package Cantera.[12] However, for simplicity, all gas compositions in the text are displayed as $H_2/H_2O/CO/CO_2(/N_2)^{eq820\ °C}$, which denotes the corresponding equilibrium composition at 820 °C. With this notation, the equilibrium composition at 820 °C, where the equilibrium constant of the RWGS is approximately 1, is used as a reference state to describe a gas mixture. Thermodynamic carbon formation was excluded for every analyzed operation point.

Impedance spectra were all recorded under OCV, acquired by a Solartron 1260 frequency response analyzer using a pseudo-potentiostatic measurement technique. The amplitude was set to ⩽12 mV regarding polarization resistance. Every measurement was performed in a frequency range between 30 mHz and 1 MHz with 12 points per decade. Every impedance measurement was performed twice: One after a stabilization time of 1.5 h with lower resolution and a second after additional 0.5 h holding time. Only if no short term-changes are observed, the spectrum is treated as valid. The second measurement was then used for analysis. Therefore, short-term ageing effects caused by unstable operation points or contaminants in the CO_x feed gases[13] could be excluded. All measured spectra were verified by a Kramers Kronig Test.[14] Distribution of relaxation times (DRT) analysis and complex-nonlinear-least-squares (CNLS) fitting was performed with in-house software.

Results and Discussion

Influence of CO and CO_2 content.—Depending on the desired product stoichiometry, various gas compositions can be fed to a solid oxide cell (SOC). On an incremental electrode at open circuit conditions, a gas mixture consisting of $H_2/H_2O/CO/CO_2$ can be fully defined by its total CO- and CO_2-content $y_{CO} + y_{CO_2}$ and its total fuel content $y_{H_2O} + y_{CO_2}$. However, when gases are not added in equilibrium the (R)WGS-reaction can cause significant gradients within the cell and current collector volume. This effect is minimized when the gas mixture sees sufficient amounts of active

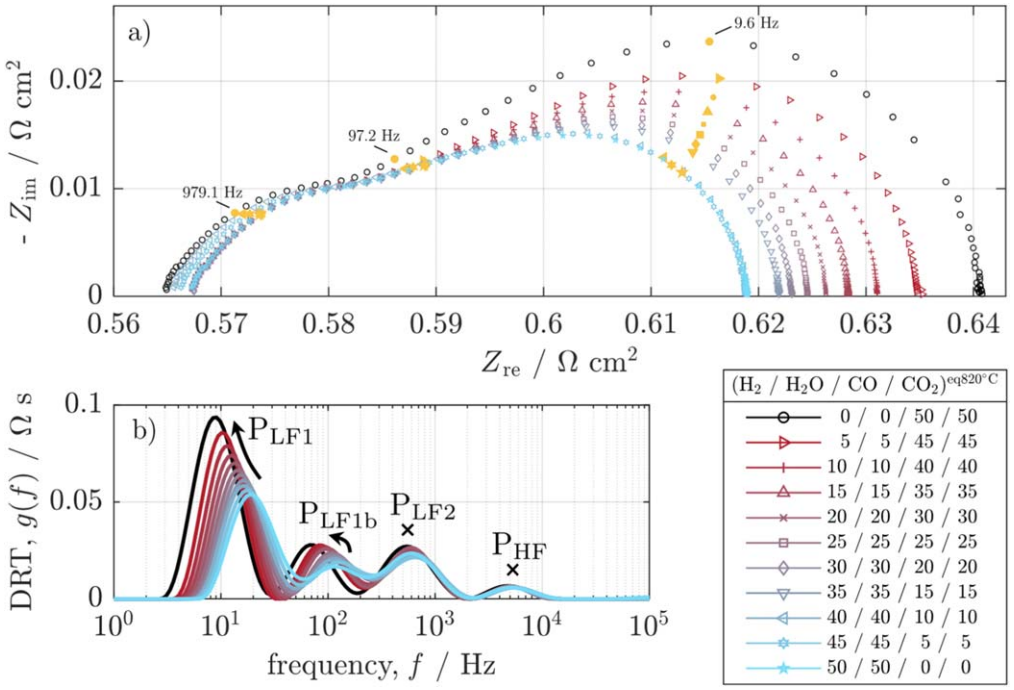

Figure 1. (a) EIS and (b) DRT plot obtained from a variation of $y_{CO} + y_{CO_2}$ at a constant fuel content of $y_{H_2O} + y_{CO_2} = 50\%$ and 860 °C.

catalyst to be equilibrated before reaching the active electrode volume. This could be the case for fuel electrode supported cells, with thick Ni containing substrates. On the other hand, equilibrium in the active electrode volume is not always ensured on electrolyte supported cells with thin current collectors. This may result in an undefined gas composition in the active electrode volume. We therefore ensured a defined fuel gas composition in the electrode volume by adding the gas mixture in its equilibrium, as previously done by Kromp et al.[1]

To investigate the influence of fuel gas composition, impedance measurements at $y_{CO} + y_{CO_2} = 0\%–100\%$ (H_2/H_2O-operation towards CO/CO_2-operation) were performed at a total fuel content of $y_{H_2O} + y_{CO_2} = 50\%$ and 860 °C. Gases were added in the corresponding equilibrium composition. Measured spectra can be seen in Fig. 1. The spectra generally consist of two arcs, one at the low frequency end of the spectrum with a peak frequency of 8–20 Hz and the other one at the high frequency end at a peak frequency of ~600 Hz, with the latter intercepting the real axis at an angle of ~50°. Subsequent DRT analysis shows four peaks for every analyzed $y_{CO} + y_{CO_2}$. It can be noticed, that an increase in $y_{CO} + y_{CO_2}$ results in an increase of polarization resistance, except for the range $y_{CO} + y_{CO_2} = 0\%–20\%$, where spectra are nearly identical. Most changes appear to be in the low frequency region (<200 Hz), while higher frequency contributions are not or only weakly influenced. Therefore, in the following, the four visible peaks in the DRT will be named, in their respective order from low frequencies towards high frequencies, as P_{LF1}, P_{LF1b}, P_{LF2} and P_{HF}.

For Ni/GDC-electrodes, it is generally believed to locate surface processes (i.e. adsorption, surface reaction) and gas diffusion contributions at lower frequencies.[4,5,7] Following this assumption, the observed increase in the low frequency resistance contributions could correspond to an increase in either gas diffusion or surface process resistances. As an increasing amount of CO and CO_2 decreases the effective gas diffusion coefficient and the charge transfer resistance for the CO-CO_2 redox couple is higher, both seem to be reasonable.[3] Bulk processes (i.e. charge transport in the bulk and at resistive interfaces) on the other hand are found at higher frequencies.[4,15,16] This agrees with the observed weak dependence of the high frequency contributions on gas atmosphere.

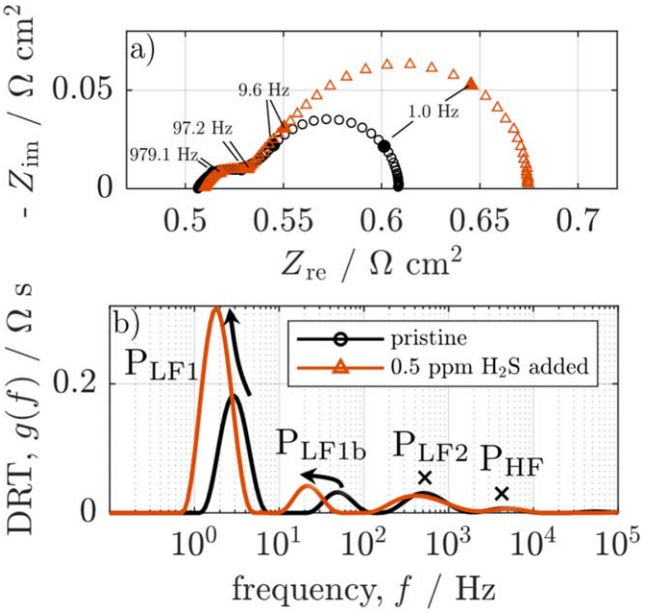

Figure 2. EIS spectra (a) and DRT plot (b) obtained before (pristine, black) and after poisoning with 0.5 ppm H_2S (orange). Spectra are recorded at OCV and 860 °C with $H_2/H_2O/CO/CO_2/N_2^{eq820\ °C} = 15/5/15/5/60$.

Influence of sulfur poisoning.—Sulfur containing species are an often-found contaminant in carbon-containing fuels,[13] i.e. natural gas or off-gases from power-plants. In the form of H_2S, sulfur at low concentrations is known to adsorb reversibly on nickel[17] as well as partly on ceria[18] and block active sites for electrochemical[18–22] and catalytic (non-faradaic)[23,24] reactions, while leaving bulk processes like charge transport inside the electrode unaffected. Thus, low concentrations of H_2S added to the fuel can help localize the frequency range of a surface process within the impedance response. It has to be considered that gas diffusion can also be affected as the catalytic water gas shift reaction on the Ni-catalyst is deactivated by sulfur.[23]

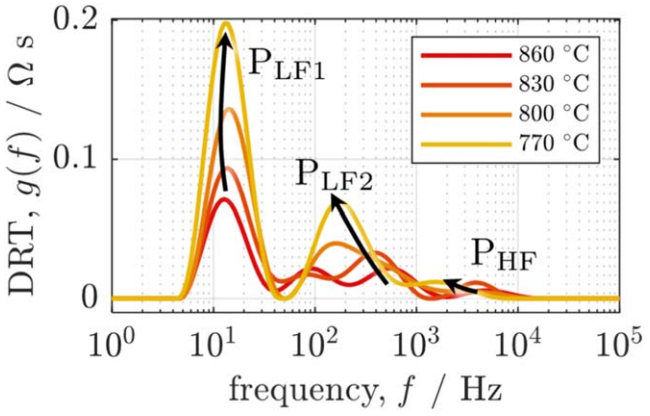

Figure 3. DRT plots obtained from temperature variation in steps of 30 K from 770 °C to 860 °C at $H_2/H_2O/CO/CO_2^{eq820\ °C}$ = 25/25/25/25.

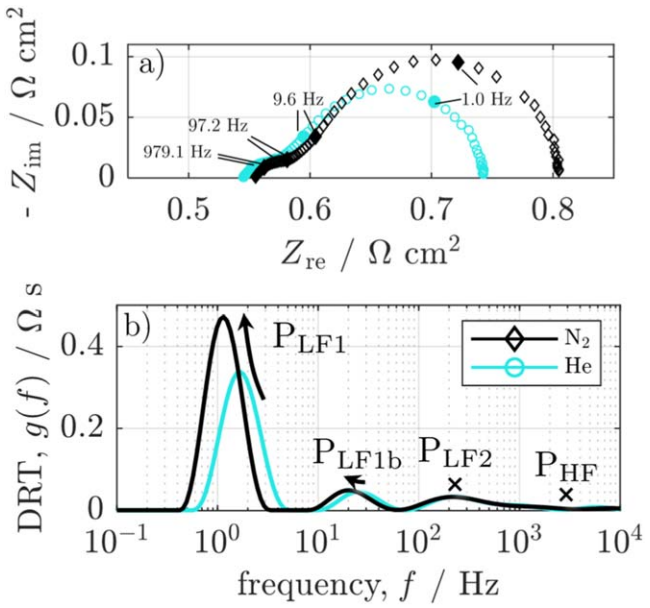

Figure 4. EIS spectra (a) and DRT plot (b) obtained from dilution with nitrogen (black) and helium (turquoise). Spectra are recorded at OCV and 870 °C at $H2/H2O/CO/CO2/(N2/He)^{eq820\ °C}$ = 5/2.5/5/2.5/85.

Following this idea, a low concentration of H_2S (0.5 ppm) was added to the fuel gas mixture. The experiment was performed at an operating point with high dilution ($H_2/H_2O/CO/CO_2/N_2^{eq820\ °C}$ =15/5/15/5/60) to enable a sufficient separation of the time constants from process P_{LF1} and P_{LF2}. The impedance response can be seen in Fig. 2a. As a result of the poisoning, an increase in polarization resistance could be observed within several hours. The observed increase is mainly found within the low frequency arc. This is in accordance with the sulfur poisoning response on Ni/GDC fuel electrodes observed by Riegraf et al.[21] DRT analysis (Fig. 2b) revealed an increase and shift to lower frequencies within P_{LF1} and P_{LF1b}, while leaving P_{LF2} and P_{HF} nearly unaffected. It follows the conclusion, that the dominant surface process contributions are located within P_{LF1} and P_{LF1b}. From this point, a clear separation between gas diffusion and surface process contributions is still not possible and shall be clarified within the following sections.

Localization of gas diffusion.—It is widely known, that charge transfer resistances as well as charge transport resistances inside SOC-electrodes and electrolytes exhibit an inverse Arrhenius temperature dependence. Gas diffusion resistances, on the other hand, show a $T^{0.5}$ dependence. Thus, a variation of temperature is often used to identify gas diffusion contributions. In the case of Ni/GDC electrodes an overlap of activation polarization and gas diffusion polarization is frequently reported in literature.[3–8] This is often attributed to the high chemical capacity of GDC, resulting in activation polarization contributions appearing at lower frequencies.

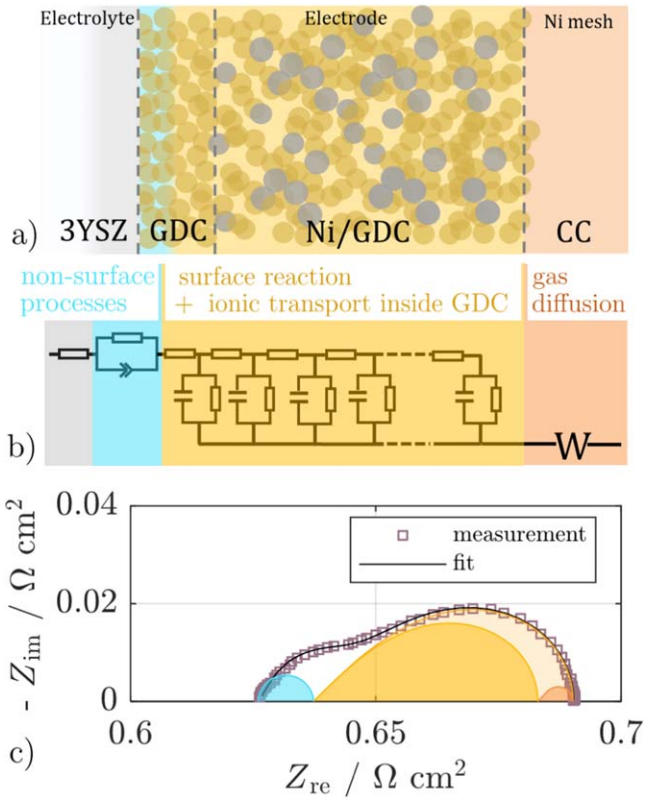

Figure 5. (a) Schematic sketch of the investigated Ni/GDC electrode with GDC interlayer between 3YSZ and Ni/GDC and Ni current collector (CC) as main source of gas diffusion resistance. (b) Derived ECM for the impedance analysis of Ni/GDC electrodes. The used ECM considers the GDC interlayer- and Ni/GDC-phase as homogenized. (c) Examplary fit at 850 °C and $H_2/H_2O/CO/CO_2^{eq820\ °C}$ = 25/25/25/25. The circuit elements are shown in (b) from left to right in the direction of high to low chracteristic frequencies, respectively, and are visualized in (c). Additionally, the formation of the low frequency arc from the overlapping TLM and Warburg element is visualized in (c).

To analyze, if a separation of gas diffusion and activation polarization is observable within our setup, a temperature variation was performed. In Fig. 3 the DRT obtained by a variation of temperature from 770 °C to 860 °C, at $H_2/H_2O/CO/CO_2^{eq820\ °C}$ = 25/25/25/25 can be seen. All visible peaks seem to rise with decreasing temperature. This is in accordance with earlier reports by Grosselindemann et al.[3,6] and Riegraf et al.,[4] stating that no process with weak temperature dependence can be found in the DRT of symmetrical Ni/GDC electrodes. However, it has to be noted that below 800 °C a separation between P_{LF1b} and P_{LF2} at these conditions is not possible, due to their weakly separated time constants.

With the goal to further locate the full gas diffusion contributions found within the obtained spectra, two measurements with either high helium or nitrogen content, at $H_2/H_2O/CO/CO_2/(N_2/He)^{eq820\ °C}$ = 5/2.5/5/2.5/85, were performed. The sole change of inert species is assumed to only influence impedance contributions related to gas diffusion, leaving any other physical process uninfluenced.[6] The resulted impedance measurement and subsequent DRT can be seen in Fig. 4. A change from nitrogen to helium as diluent results in a lower polarization resistance, which is due to faster multicomponent gas diffusion through helium. In the DRT in Fig. 4b it can be seen, that P_{LF1} as well as P_{LF1b} are influenced by the change of inert

diluent. P_{LF1} shows a significant decrease in size and an increase in peak frequency, while P_{LF1b} showing a rather insignificant decrease in size, but a visible increase in peak frequency. P_{LF2} as well as P_{HF} are not influenced by the change of diluent. It follows, that P_{LF1} results from a superposition of a temperature activated surface process and a gas diffusion contribution. Similar conclusions were drawn by Riegraf et al., for operation under steam and hydrogen.[4] Considering that both, gas diffusion and the coupling of charge transfer and ionic transport, can be described by transmission line type models (Warburg element and single channel transmission line) that both exhibit satellite peaks at higher frequencies,[25] P_{LF1b} is also affected by gas diffusion and activation polarization. Motivated by the observed findings, a suitable equivalent circuit model (ECM) is derived in the following section.

Derivation of equivalent circuit model.—From the above discussed results, the ECM displayed in Fig. 5b is derived, which is used for complex-nonlinear-least-squares (CNLS) fitting. An ohmic resistance (R_0) accounts for the ohmic contributions arising from the 3YSZ electrolyte as well as from the electrode.[26] P_{LF2} is dominantly resulting from a process which is not related to the surface, i.e. from the 3YSZ|GDC interface[5] and bulk processes[4] close to the interface, as it only exhibits a low dependence on gas phase conditions. To clarify the actual origin of P_{LF2}, further experiments with specifically designed model electrodes would be necessary, but these experiments are beyond the scope of this work. A resistance parallel to a constant-phase-element (R||CPE) therefore accounts for the main part of P_{LF2}, which is assumed to be fully decoupled from any process inside the electrode layers. P_{LF1} and P_{LF1b} show a strong dependence on gas phase conditions. Also, they are strongly influenced by sulfur poisoning. Thus, they comprise the dominant contributions of a thermally activated surface process in superposition with a gas diffusion process. They are modelled via a transmission line model (TLM) with omitted electronic resistance and a Warburg element in series. Hence, they account for the electrochemical surface reaction coupled with the ionic transport inside the GDC matrix and the gas diffusion resistance, respectively. An overview of the identified processes and their frequency ranges can be found in Table I.

Generally, the impedance of a porous electrode with an electronically conducting phase and an ionically conducting phase can be described by a transmission line circuit.[25] The transmission line consists of an electronic rail and an ionic rail, each associated with their incremental impedance contribution χ_{el} and χ_{ion}, respectively. The coupling of the rails is realized via the incremental impedance ζ accounting for the charge transfer between the two phases, driven by the local potential difference of the two rails. The general expression for the impedance of this transmission line circuit for an electrode with thickness L is given as[27]

$$Z = \frac{\chi_{el}\chi_{ion}}{\chi_{el}+\chi_{ion}}\left[L + \frac{2\lambda}{\sinh\left(\frac{L}{\lambda}\right)}\right] + \lambda\frac{\chi_{el}^2+\chi_{ion}^2}{\chi_{el}+\chi_{ion}}\coth\left(\frac{L}{\lambda}\right), \quad [4]$$

with

$$\lambda = \sqrt{\frac{\zeta}{\chi_{el}+\chi_{ion}}}. \quad [5]$$

The applicability of the transmission line approach is not only limited to electrodes with two separate conducting phases, but has been used to successfully model the impedance of single phase MIECs[28] and MIEC-electrodes.[10]

In the case of cermet electrodes, on the other hand, the impedance of the electronic rail can be omitted, due to the high electronic conductivity of the metallic phase. The expression simplifies to

$$Z = \lambda\chi_{ion}\coth\left(\frac{L}{\lambda}\right), \quad [6]$$

with the penetration depth

$$\lambda = \sqrt{\frac{\zeta}{\chi_{ion}}}, \quad [7]$$

where λ denotes the distance from the electrolyte towards the volume fraction of the electrode where 63% of charge transfer current has occurred. Typically, the incremental impedance of the ionic rail is treated as an ohmic resistor per unit length (r_{ion}). Multiplied by the cell area A_{cell}, the value is inversely proportional to the effective ionic conductivity $\sigma_{ion,eff}$ of the cell:

$$\chi_{ion} = r_{ion} = \frac{1}{\sigma_{ion,eff}}\cdot\frac{1}{A_{cell}}. \quad [8]$$

Depending on the modelled system, the impedance between the electronic and the ionic rail ζ is associated with a different resistance contribution. In the case of Ni/YSZ cermet electrodes ζ is associated with the charge transfer resistance at the triple phase boundary and the double layer capacitance between nickel and YSZ.[29,30] In the case of single phase MIEC electrodes ζ is rather associated with the surface reaction resistance at the double phase boundary and the chemical capacitance of the electrode material.[31] For very thick electrodes ($L \gg \lambda$) the impedance expression results in the well-known Gerischer impedance.[25] For Ni/GDC electrodes, both cases seem to be reasonable as there is a possibility for triple and double phase boundary reactions.[32] In this study, we use the more general terms surface reaction resistance r_{SR} and chemical capacitance c_{chem}, which can in principle result from a superposition of both mechanisms. Thus, the charge transfer impedance is modelled by a simple RC element containing r_{SR} and c_{chem}:

$$\zeta = \frac{r_{SR}}{1 + i\omega r_{SR}c_{chem}}. \quad [9]$$

Rather similar ECMs were previously used by Nenning et al. and Kullmann et al. to describe the impedance response of a Ni/GDC cermet and a single phase GDC electrode, respectively.[5,10] An

Table I. Identified Peaks from DRT analysis, with their respective frequency ranges and proposed physical assignment.

Peak	Frequency range	Dependencies	Physical assignment
P_{LF1}	0.03–60 Hz	$y_{CO}+y_{CO_2}$, H_2S, N_2 vs He, T	Surface reaction coupled with ionic transport + gas diffusion process
P_{LF1b}	30–200 Hz	$y_{CO}+y_{CO_2}$, H_2S, N_2 vs He, T-dependency unclear	Surface reaction coupled with ionic transport + gas diffusion process
P_{LF2}	100–2000 Hz	T	Bulk charge transport inside GDC close to the interface and/or resistive interfacial processes
P_{HF}	>2 kHz	T	Bulk charge transport inside GDC close to the interface and/or resistive interfacial processes

exemplary fit under $H_2/H_2O/CO/CO_2^{eq820\ °C} = 25/25/25/25$ and 850 °C with the visualized circuit elements can be seen in Fig. 5c. As shown in Fig. 6, the obtained fitting results visually agree well with the data under H_2/H_2O-, CO/CO_2- as well as $H_2/H_2O/CO/CO_2$ atmospheres. Only for the H_2/H_2O-case, the time constant of P_{LF1b} is insufficiently represented in the fit and it thus merges into a single peak with P_{LF2}. Possibly, the slight inaccuracy results from the homogenization of the GDC- and Ni/GDC-layer in the fitting approach. However, the actual deviation from the measurement data in the respective frequency region is still <0.2%. In all cases, fitting residuals were below 1%.

The advantage of such transmission line ECMs is the physical meaningfulness of the obtained fitting parameters compared to classical multi-(R||CPE) circuits. Its resistance between the ionic and electronic rail (r_{SR}) of the TLM is directly related to the surface reaction resistance. Thus, its value and correlation to operating conditions is a useful measure for the dominant electrochemical pathway of the surface reaction. However, the TLM would be overparametrized with the ionic resistance (r_{ion}), the chemical capacitance (c_{chem}) and surface reaction resistance (r_{SR}) left as free fitting parameters. As to obtain unique fitting parameters, one of the described values needs to be determined experimentally[10,29] or estimated appropriately.[5] The ionic resistance was therefore estimated appropriately and kept fixed during fitting, as described in the following section.

Estimation of r_{ion}.—The ionic resistance can be described as the inverse of the effective ionic conductivity ($\sigma_{ion,GDC,eff}$) of GDC as the ionically conducting phase

$$\frac{1}{r_{ion}} = \sigma_{ion,GDC,eff} \cdot A_{cell} = A_{cell} \cdot \frac{\varepsilon_{GDC}}{\tau_{GDC}} \cdot \frac{\sigma_{0,ion,GDC}}{T} \cdot \exp\left(-\frac{E_{a,ion,GDC}}{\tilde{R}T}\right), \quad [10]$$

with ε_{GDC} and τ_{GDC} denoting the microstructural parameters volume fraction and tortuosity of GDC, respectively. $E_{a,ion,GDC}$ represents the activation energy of the ionic conductivity, $\sigma_{0,ion,GDC}$ the preexponential factor and $\tilde{R}$ the universal gas constant. Microstructural parameters are accessible through focused ion beam scanning electron microscope (FIB-SEM) tomography. Furthermore, the preexponential factor $\sigma_{0,ion,GDC}$ and the activation energy $E_{a,ion,GDC}$ can be obtained by 4-point DC conductivity measurements[10,29] as well as impedance spectroscopy[33–35] of bulk GDC samples. The actual values of $\sigma_{0,ion,GDC}$ and $E_{a,ion,GDC}$ depend highly on dopant content,[35] p_{O_2},[36] preparation technique[34] and the micro- and nanostructure of the electrode.[32]

In this work, the bulk conductivity of GDC was estimated from data reported by Kullmann et al.[10] They measured the conductivity of porous GDC20 between 600 °C and 700 °C. To yield values for higher temperatures, their data was fitted with an Arrhenius approach according to Eq. 10 and extrapolated towards 860 °C. For consideration of GDC oxygen nonstoichiometry[33,36] the same approach as by Kullmann et al.[10] is used. Their approach is based on nonstoichiometry data reported by Bishop et al.[37] and a method for deconvoluting electronic and ionic conductivity of GDC developed by Wang et al.[33] For calculation of the effective ionic conductivity $\sigma_{ion,GDC,eff}$ of our sample, a FIB-SEM reconstruction was performed. The reconstruction of the GDC and Ni/GDC layer yielded a total (homogenized) value of $\frac{\varepsilon_{GDC}}{\tau_{GDC}} = 0.316$. For detailed information on FIB-SEM reconstruction of cermet electrodes, we refer to the work of Kullmann et al. and Joos et al.[10,38] The exact values used for parametrization of the transmission line model are listed in Table II.

Estimation of R_{Diff}.—Depending on the setup, flow rate and cell geometry, gas diffusion resistances can have a significant impact on impedance measurements and cell performance. Aravind et al. used

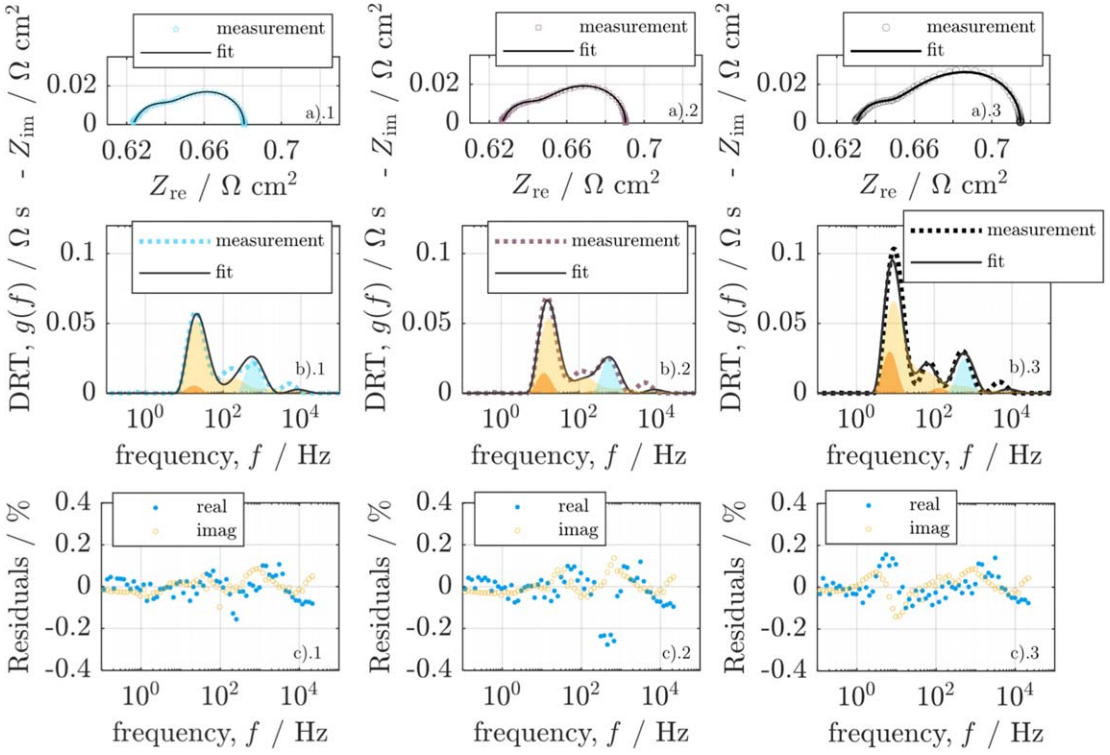

Figure 6. (a) Examplary EIS spectra recorded at 850 °C with fit, (b) DRT constructed from measurement data and fit with circuit elements as area plots in the color code given in Fig. 5 and (c) corresponding residuals at $H_2/H_2O/CO/CO_2^{eq820\ °C} = 50/50/0/0$ (a-c.1), $H_2/H_2O/CO/CO_2^{eq820\ °C} = 25/25/25/25$ (a-c.2) and $H_2/H_2O/CO/CO_2^{eq820\ °C} = 0/0/50/50$ (a-c.3). The fit yields excellent agreement with measurement data under every analyzed gas atmosphere. Residuals are in every case below 1%.

Table II. Estimates of bulk ionic conductivities $\sigma_{ion,GDC}$ and resulting ionic resistances r_{ion} at the investigated temperatures and p_{O_2} ranges used for TLM parametrization.

T/°C	p_{O_2}/atm	$\sigma_{ion,GDC}$/S cm^{-1}	r_{ion}/Ω cm^{-1}
780	1.1…1.6 × 10^{-19}	0.035	89.6
790	2.1…2.6 × 10^{-19}	0.039	81.2
800	3.5…4.5 × 10^{-19}	0.043	73.8
810	6.8…7.5 × 10^{-19}	0.047	67.1
820	1.2…1.2 × 10^{-18}	0.052	61.1
830	2.0…2.1 × 10^{-18}	0.057	55.6
840	3.3…3.7 × 10^{-18}	0.063	50.8
850	5.3…6.4 × 10^{-18}	0.068	46.4
860	0.9…1.1 × 10^{-17}	0.075	42.4

1 mm thick ceramic supports to create a big stagnant diffusion layer on top of electrolyte supported Ni/GDC symmetric cells and measured gas diffusion resistances comprising more than 50% of the total polarization resistance at 850 °C.[39] In a recent publication by Unachukwu et al., gas diffusion resistances of ∼0.06 Ω cm^2 at a total polarization resistance of ∼0.13 Ω cm^2 were measured in a setup with electrolyte supported full cells with Ni/GDC fuel electrode under CO_2/CO/H_2O atmospheres and 850 °C.[40] The authors were able to directly fit the diffusion resistance with a Warburg element as the gas diffusion did not overlap with activation resistance contributions, which was speculated to be due to the fact that their cell did not comprise a GDC layer between Ni/GDC and electrolyte. Nevertheless, multiple studies investigating Ni/GDC electrodes with and without GDC interlayer demonstrated an overlap of gas diffusion and activation resistances,[3–8] thus gas diffusion resistances cannot be extracted directly from impedance measurements. To calculate the gas diffusion resistance R_{Diff}, the following formula, developed by Primdahl and Mogensen can be used:[41]

$$R_{Diff} = \left(\frac{\tilde{R}T}{2F}\right)^2 L_{Diff}\left(\frac{1}{D_{eff,r}y_r} + \frac{1}{D_{eff,ox}y_{ox}}\right)\frac{1}{P}, \quad [11]$$

with R_{Diff} being gas diffusion resistance, $\tilde{R}$ the gas constant, T temperature, F the Faraday constant, L_{Diff} the diffusion length, P the overall system pressure, $D_{eff,i}$ the effective diffusion coefficient and y_i the molar fraction of either reduced component r or oxidized component ox. This formula is widely utilized and can be used for binary[4] as well as for ternary gas mixtures[3,6,39] containing only one redox-couple. In the case of multicomponent gas mixtures with more than one redox-couple it is not possible to directly apply this formula. To account for the two redox-couples present under H_2/H_2O/CO/CO_2-atmospheres, we propose the equation

$$R_{Diff} = \left(\frac{RT}{2F}\right)^2 L_{Diff}\left[\left(\frac{1}{D_{eff,CO}y_{CO}} + \frac{1}{D_{eff,CO_2}y_{CO_2}}\right)^{-1} + \left(\frac{1}{D_{eff,H_2}y_{H_2}} + \frac{1}{D_{eff,H_2O}y_{H_2O}}\right)^{-1}\right]^{-1}\frac{1}{P}, \quad [12]$$

which can be seen as the resulting resistance of a parallel circuit incorporating two resistors, each representing a gas diffusion resistance from the redox couples H_2/H_2O and CO/CO_2 (Fig. 7).

For electrolyte supported cells, it is common to neglect gas diffusion in the pores of the thin electrode layer as the electrode thickness (∼20 μm) is small compared to the thickness of the Ni contact mesh (∼240 μm) on top of the electrode.[4] Knudsen diffusion inside the Ni contact mesh can also be neglected, due to its open structure with pore diameters of around 250 μm and mean free path lengths of 292 nm (CO_2, 800 °C) to 453 nm (H_2O, 800 °C). Thus, Eq. 12 can be simplified to

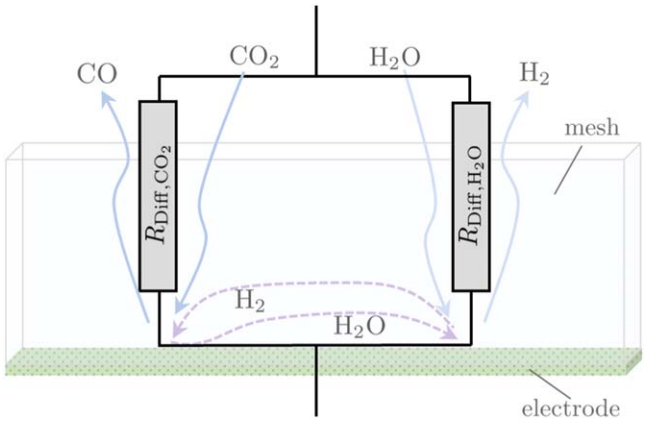

Figure 7. Schematic representation of gas diffusion mechanism according to Eq. 12. Simultaneous gas diffusion of the CO-CO_2 couple and the H_2-H_2O couple is treated as two parallel gas diffusion resistances, while the (R)WGS reaction is considered to occur close to the electroactive zone.

$$R_{Diff} = \left(\frac{RT}{2F}\right)^2 G_{eff}^{-1}\left[\left(\frac{1}{D_{mol,CO}y_{CO}} + \frac{1}{D_{mol,CO_2}y_{CO_2}}\right)^{-1} + \left(\frac{1}{D_{mol,H_2}y_{H_2}} + \frac{1}{D_{mol,H_2O}y_{H_2O}}\right)^{-1}\right]^{-1}\frac{1}{P}, \quad [13]$$

with molar diffusion coefficients $D_{mol,i}$ of the corresponding species i. Molar diffusion coefficients in multicomponent gas mixtures can be obtained as proposed by Wilke,[42] required binary diffusion coefficients can be calculated by Chapman-Enskog-theory.[43] The geometry parameter is further defined as:[6]

$$G_{eff} = \frac{\Psi}{L_{Diff}}, \quad [14]$$

where Ψ is the microstructure parameter within the gas diffusion layer. By applying the method proposed by Grosselindemann et al.[6] the geometry parameter was estimated to be G_{eff} = 805 m^{-1}, which is close to the value of 734 m^{-1} they have reported. The values then yielded from Eq. 13 are listed in Table III.

Influence of $y_{CO} + y_{CO_2}$ on r_{SR}.—With the above discussed assumptions, a CNLS fitting procedure has been developed to determine r_{SR} for every H_2/H_2O/CO/CO_2-mixture from Fig. 1. The procedure is as follows: The gas diffusion resistance R_{Diff} is predefined and calculated according to Eq. 13. r_{ion} is assumed to be constant at one given temperature and predefined from conductivity-, GDC-nonstoichiometry- and FIB-SEM-reconstruction-data, as in more detail described above.

However, R_{LF2} cannot be easily calculated a priori, therefore it has to be fitted to experimental data. Even though the close time constants of P_{LF2} and P_{LF1b} impose a challenge for accurate fitting, especially at temperatures <800 °C, a unique result of R_{LF2} is still obtainable, due to the used transmission line approach. The size and frequency of the second peak produced by the transmission line model (P_{LF1b}) is dominated by r_{ion} and only weakly influenced by r_{SR}.[44] As r_{ion} is calculated before fitting, the result of R_{LF2} can be considered to be accurate. To further ensure a precise result of R_{LF2}, it is assumed to be constant for every analyzed gas atmosphere at one given temperature. The preceding DRT-analysis showed, that P_{LF2} is independent from changes in gas atmosphere and fully decoupled from surface contributions, thus the assumption of a gas phase independent R_{LF2} can be considered valid.

To realize a gas phase independent R_{LF2}, we perform the CNLS fit on multiple spectra (obtained at different gas phase conditions) at

Table III. Simulated R_{Diff} for every investigated temperature and $y_{CO} + y_{CO_2}$ calculated by Eq. 13 and multiplied by two to correct for the symmetrical cell impedance. The values are used as fixed parameters for the resistance values of the Warburg element in the circuit displayed in Fig. 5b.

$y_{CO} + y_{CO_2}$ /%	R_{Diff}/mΩcm^2								
	780 °C	790 °C	800 °C	810 °C	820 °C	830 °C	840 °C	850 °C	860 °C
0	2.7	2.7	2.7	2.7	2.7	2.8	2.8	2.8	2.8
10	3.7	3.7	3.7	3.7	3.8	3.8	3.8	3.8	3.8
20	4.6	4.6	4.7	4.7	4.7	4.7	4.7	4.7	4.7
30	5.5	5.5	5.5	5.5	5.5	5.5	5.5	5.6	5.6
40	6.3	6.3	6.3	6.3	6.4	6.4	6.4	6.4	6.4
50	7.2	7.2	7.2	7.2	7.2	7.2	7.2	7.2	7.3
60	8.1	8.1	8.1	8.1	8.1	8.2	8.2	8.2	8.2
70	9.2	9.2	9.2	9.2	9.2	9.2	9.3	9.3	9.3
80	10.5	10.5	10.5	10.6	10.6	10.6	10.6	10.6	10.7
90	12.3	12.3	12.3	12.4	12.4	12.4	12.4	12.5	12.5
100	14.8	14.8	14.9	14.9	15.0	15.0	15.1	15.1	15.1

once, while allowing only one solution for the (R|CPE)-Element describing P_{LF2}. In that way a single common cost function for 11 spectra ($y_{CO} + y_{CO_2}$= 0%–100% in 10% steps) is minimized at every temperature step. The remaining change in the spectra can then be fully attributed to the change in r_{SR}. This facilitates a meaningful analysis of the surface reaction.

The evolution of r_{SR} over an increase of $y_{CO} + y_{CO_2}$ obtained from fitting with the described technique at 860 °C, 820 °C and 780 °C is shown in Fig. 8. For all temperatures it can be seen, that the surface reaction resistance is lowest in the range $y_{CO} + y_{CO_2}$= 0%–20%, where r_{SR} remains practically unchanged. By increasing $y_{CO} + y_{CO_2}$ a gradual increase in surface reaction resistance is observable: between $y_{CO} + y_{CO_2}$= 20%–60% the increase in r_{SR} follows a linear trend. Linear fits in the region $y_{CO} + y_{CO_2}$= 20%–60% yielded R^2-values >0.99 for all temperatures, with increasing slopes towards lower temperatures. At $y_{CO} + y_{CO_2} \geqslant$ 70% the increase in r_{SR} is exponential. The CO/CO_2-case shows the highest r_{SR}, exhibiting at 860 °C a 60% larger value compared to the H_2/H_2O-case. Thus, three regimes can be identified: a constant regime in the range $y_{CO} + y_{CO_2}$= 0%–20%, a linear regime in the region $y_{CO} + y_{CO_2}$= 20%–60% and an exponential regime for $y_{CO} + y_{CO_2} \geqslant$ 70%.

Generally, higher activation losses under CO/CO_2-atmospheres compared to H_2/H_2O atmospheres are a known phenomenon for GDC based electrodes[3,6,40,45–47] as well as for Ni/YSZ based electrodes,[2,48,49] thus the observed result is in accordance with literature.

In the results presented by Ioannidou et al., addition of CO_2 to an H_2/H_2O/He mixture caused no significant changes in polarization resistance up to a CO_2/(H_2+H_2O) ratio of 1/2 at 900 °C.[50] This agrees well with the observed constant regime in the range $y_{CO} + y_{CO_2}$= 0%–20%. It can be concluded, that in this regime the very fast (R)WGS enables a nearly loss free exchange of oxygen between C-species and H-species before the H-species are electrochemically converted.

Interestingly, a significant increase in polarization resistance with increasing $y_{CO} + y_{CO_2}$ at the identical boundary of $y_{CO} + y_{CO_2}>$ 70% was observed by Wolf et al. on fuel electrode supported Ni/YSZ electrodes.[2] This was attributed to the onset of the electrochemical CO_2 reduction, while RWGS + electrochemical H_2O reduction was suspected to be dominant in the region $y_{CO_2}<$ 70%. As the electrode analyzed in this study is significantly thinner (~20 μm) compared to the one analyzed by Wolf et al. (~300 μm), it contains less nickel and thus a slower overall (R)WGS-rate is expected.[51] As we observe a very similar behavior at the same $y_{CO} + y_{CO_2}$, one may conclude that possibly Ni/GDC has a higher

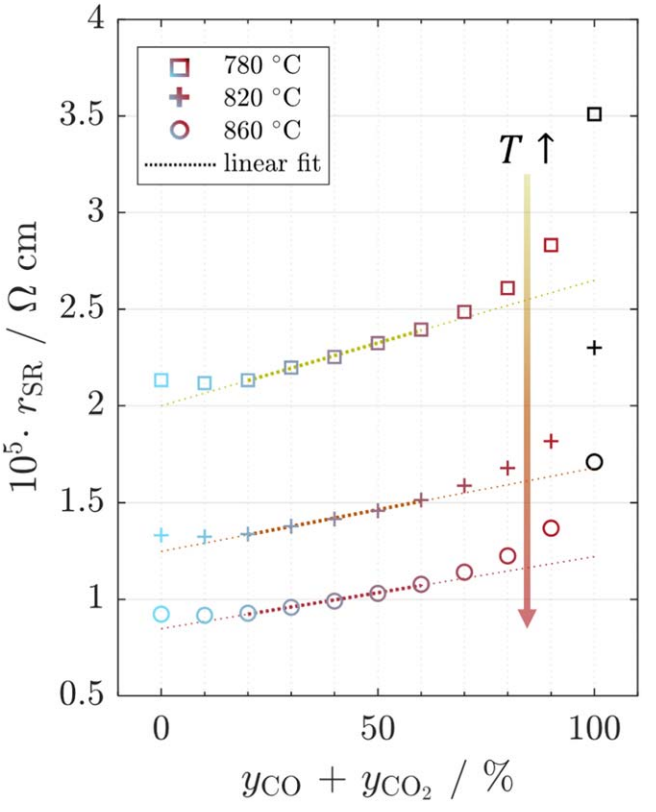

Figure 8. Evolution of r_{SR} over $y_{CO} + y_{CO_2}$ at 860 °C, 820 °C and 780 °C at a constant fuel content of $y_{H_2O} + y_{CO_2}$= 50%. Linear fits were performed in the range $y_{CO} + y_{CO_2}$ = 20%–60% and yielded R^2 > 0.99 for all temperatures. Fits are extrapolated towards lower and higher $y_{CO} + y_{CO_2}$ to indicate the deviation from linearity in the constant and exponential regime.

(R)WGS-activity compared to Ni/YSZ, enabling similar (R)WGS rates despite the smaller electrode volume. This seems reasonable as ceria oxides have a higher catalytic RWGS activity compared to YSZ,[52] metallic catalysts supported on doped ceria show a higher RWGS activity than those supported on YSZ[53] and the addition of ceria to Al_2O_3 supported Ni catalysts increases their WGS-activity.[54]

However, changes in the linear regime are much harder to interpret and a very clear boundary for the onset of the electrochemical CO/CO_2-conversion cannot be easily identified from Fig. 8. Increasing slopes of the linear fit may be caused by the

different activation energies of the electrochemical CO/CO_2- and H_2/H_2O-conversion, which would indicate an influence of the CO/CO_2 electrochemistry at $y_{CO} + y_{CO_2} < 70\%$. To further investigate this, the temperature dependency of r_{SR} at different $y_{CO} + y_{CO_2}$ is analyzed in the following chapter.

Electrode kinetics.—The temperature dependence of R_0, R_{LF2} and r_{SR} under every $H_2/H_2O/CO/CO_2$-mixture from Fig. 1 was analyzed in a temperature range of 780 °C–860 °C. The temperature dependency of R_0 and R_{LF2} is plotted in Fig. 9a. The activation energy of the ohmic resistance shows no dependency on $y_{CO} + y_{CO_2}$ and resulted in 79.8–80.2 kJ mol^{-1}. The value is in perfect accordance with the results obtained by Grosselindemann et al.[6] (85 kJ mol^{-1} at 800 °C). Furthermore, the temperature dependence of R_{LF2} was analyzed and resulted in 78.9 kJ mol^{-1}.

In Fig. 9b the penetration depth over changing $y_{CO} + y_{CO_2}$ is plotted. The values range between 4.7 μm to 6.3 μm. The overall trend over $y_{CO} + y_{CO_2}$ qualitatively represents the course of the charge transfer resistance in Fig. 7. It can be seen, that the penetration depth increases with increasing $y_{CO} + y_{CO_2}$, which is in accordance with results by Nenning et al.[26] For all gas mixtures the penetration depth lies significantly below the overall thickness of the active electrode (15 μm).

The evolution of r_{SR} under $y_{CO} + y_{CO_2} = 0$, 30, 50, 90 and 100% over temperature is plotted in Fig. 9c. Generally, it can be seen that the CO/CO_2 mixture exhibits a higher r_{SR} than the H_2/H_2O-mixture in the total measured temperature range. With decreasing temperature, the deviation in the semilogarithmic plot between the CO/CO_2-case and the H_2/H_2O case seems to increase, thus showing

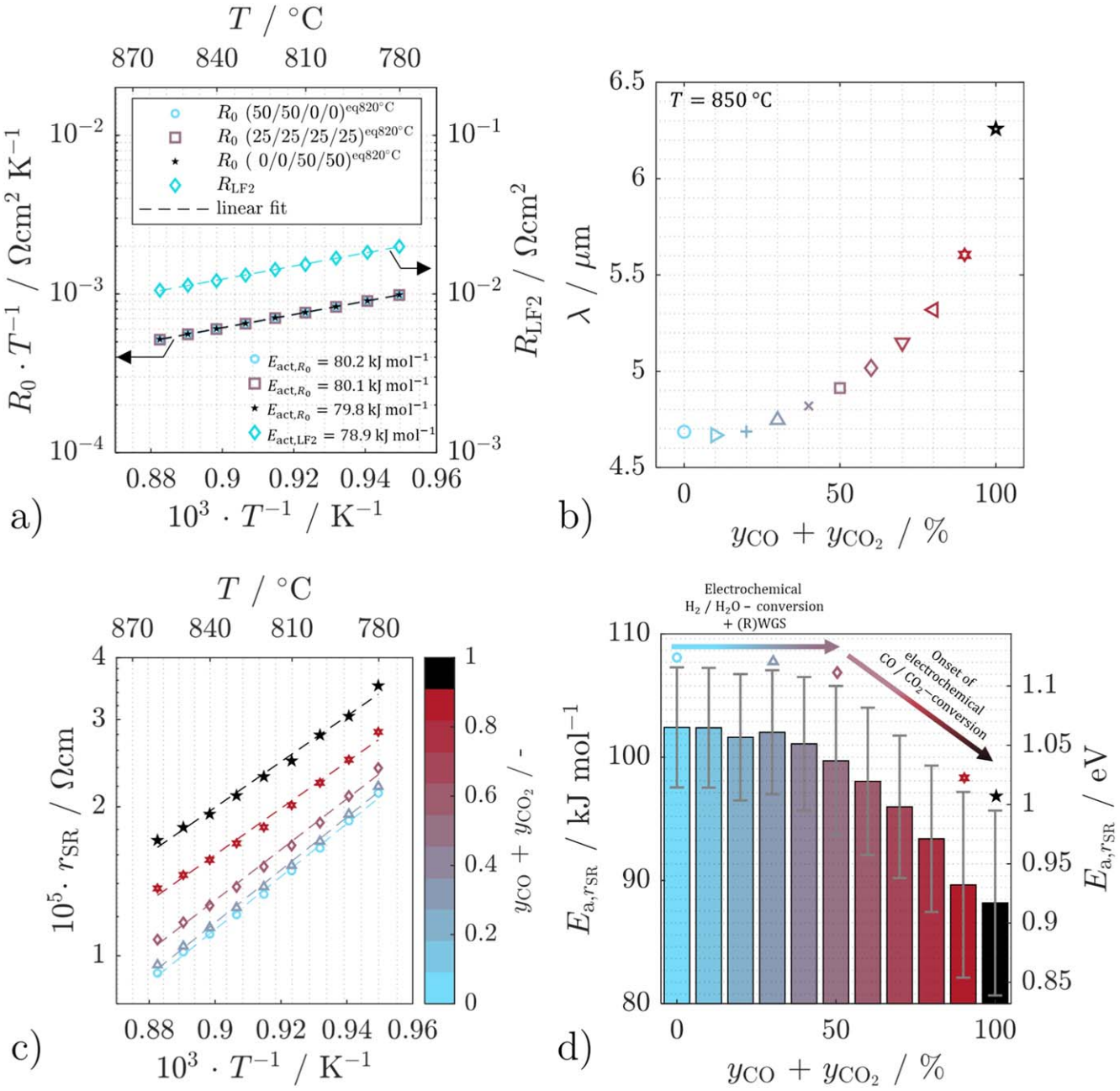

Figure 9. (a) Arrhenius plot of R_0 measured under $y_{CO} + y_{CO_2} = 0\%$, 50%, 100% and R_{LF2}. Values are extracted from the total symmetrical cell impedance. (b) The evolution of the penetration depth λ at 850 °C with varying $y_{CO} + y_{CO_2}$. (c) Arrhenius plot of r_{SR} from measurements at $y_{CO} + y_{CO_2} = 0\%$–100%. For clarity, not every measured $y_{CO} + y_{CO_2}$ is plotted. (d) The activation energies obtained from arrhenius analysis of r_{SR} plotted over $y_{CO} + y_{CO_2}$. Error bars display the 95% confidence intervals from the Arrhenius fits. Symbols above the error bars signify the compositions which were used to obtain data displayed in (c).

a lower activation energy under CO/CO_2-atmosphere than under H_2/H_2O-atmosphere. Similar observations were reported by Ioannidou et al. and Unachukwu et al. with Ni/GDC-cermet electrodes[40,47,50] as well as by Uecker et al. with single-phase GDC electrodes.[45,46] For better visualization, the evolution of $E_{a,SR}$ over $y_{CO} + y_{CO_2}$ is plotted in Fig. 9d. It can be seen that differences in $E_{a,SR}$ with increasing $y_{CO} + y_{CO_2}$ are completely neglectable up to a $y_{CO} + y_{CO_2} = 50\%$ compared to the H_2/H_2O case (99–103 kJ mol^{-1}). This indicates that the linear increase of r_{SR} up to $y_{CO} + y_{CO_2} < 60\%$ may not be caused by electrochemical CO/CO_2-conversion. A plausible explanation in this range could be concentration effects possibly caused by competitive adsorption of C-species and H-species.[55] Assuming the surface reaction resistance to be inversely proportional to the exchange current density of the reaction:[48]

$$\frac{1}{r_{SR,OCV}} \propto j_0 = \gamma p_{H_2}^{a} p_{H_2O}^{b} \exp\left(-\frac{E_{a,SR}}{\tilde{R}T}\right), \quad [15]$$

this would correspond to a change in the preexponential concentration dependent factors $\gamma p_{H_2}^{a} p_{H_2O}^{b}$, which implicitly contain the available electrochemical surface area and coverage with electrochemically active species. Generally, it can be observed that the difference in activation energy of r_{SR} under a H_2/H_2O atmosphere and a CO/CO_2 atmosphere is rather small (103 vs 88 kJ mol^{-1}). Still, from 60% on towards higher $y_{CO} + y_{CO_2}$ a more significant decrease in activation energy is observed and this trend gradually magnifies towards the CO/CO_2-case. Therefore, we conclude that up to $y_{CO} + y_{CO_2} \leqslant 50\%$ the dominant electrochemical pathway under $H_2/H_2O/CO/CO_2$-atmosphere is equivalent to the one under H_2/H_2O atmospheres and electrochemical conversion of CO/CO_2 can be neglected in this region. From $y_{CO+CO_2} \geqslant 60\%$ a possible onset of the electrochemical CO/CO_2-conversion can be detected from the observed decrease in activation energy. Additional confirmation of these findings through gas-chromatography analysis is planned and will be detailed in an upcoming publication.

Conclusions

Within this contribution, a parameter variation and a quantitative analysis of the electrode kinetics of symmetrical cells with Ni/GDC electrodes under $H_2/H_2O/CO/CO_2$-atmospheres were performed. Based on the parameter variation and DRT aided data analysis, frequency ranges for surface associated and non-surface related processes were identified. The identified frequency ranges and corresponding peaks in the DRT were:

- P_{LF1} (0.03–60 Hz): Contributions from surface process coupled with ionic transport in superposition with a gas diffusion process.
- P_{LF1b} (30–200 Hz): Contributions from surface process coupled with ionic transport in superposition with a gas diffusion process.
- P_{LF2} (100–2000 Hz): Not surface related, possibly bulk charge transport inside GDC close to the interface or interfacial processes.
- P_{HF} (>2 kHz): Not surface related, possibly bulk charge transport inside GDC close to the interface or interfacial processes.

Derived from the observed parameter dependencies, a physically meaningful equivalent circuit, including a TLM for the porous electrode impedance, was set up to quantitatively determine the electrode kinetics under varying $H_2/H_2O/CO/CO_2$-atmospheres. To avoid overparameterization, a method for estimating gas diffusion resistances under $H_2/H_2O/CO/CO_2$-atmospheres was developed. Furthermore, ionic conductivity of bulk-GDC was appropriately estimated with literature data, considering GDC oxygen nonstoichiometry. Effective conductivities were calculated through quantification of the microstructure by FIB-SEM tomography. The method enabled the direct extraction of the surface reaction resistance changes under $H_2/H_2O/CO/CO_2$-atmospheres with varying $y_{CO} + y_{CO_2}$. It was shown, that for increasing $y_{CO} + y_{CO_2}$ the surface reaction resistance does not change in the range of $y_{CO} + y_{CO_2} = 0\%–20\%$, rises linearly up to $y_{CO} + y_{CO_2} = 60\%$ and grows exponentially within $y_{CO} + y_{CO_2} = 70\%–100\%$. An analysis of the activation energies of the surface reaction resistance under the analyzed $H_2/H_2O/CO/CO_2$-atmospheres showed nearly identical activation energies in the range of $y_{CO} + y_{CO_2} = 0\%–50\%$ and a visible decrease in the range of $y_{CO} + y_{CO_2} = 60\%–100\%$. We concluded, that in the range of $y_{CO} + y_{CO_2} = 0\%–20\%$ electrochemical H_2/H_2O conversion is dominant and CO/CO_2 conversion predominantly happens via (R)WGS. In the range of $y_{CO} + y_{CO_2} = 20\%–50\%$ electrochemical CO/CO_2 conversion is not detectable, but possibly competitive adsorption of C-species and H-species could be responsible for an increase in resistance with increasing $y_{CO} + y_{CO_2}$. For $y_{CO} + y_{CO_2} \geqslant 60\%$ an onset of the electrochemical CO/CO_2-reduction was identified.

Acknowledgments

The authors gratefully acknowledge funding from the Federal Ministry of Education and Research (BMBF 03HY124C). Sincere thanks are given to Kerafol GmbH for providing the electrolyte substrates.

ORCID

D. Esau https://orcid.org/0000-0001-8386-1030
C. Grosselindemann https://orcid.org/0000-0002-9965-843X
F. Kullmann https://orcid.org/0000-0002-6653-5601
A. Lindner https://orcid.org/0000-0003-4903-3754
Z. Liang https://orcid.org/0000-0001-8265-7599
A. Weber https://orcid.org/0000-0003-1744-3732

References

1. A. Kromp, A. Leonide, A. Weber, and E. Ivers-Tiffée, *J. Electrochem. Soc.*, **158**, B980 (2011).
2. S. E. Wolf et al., *J. Electrochem. Soc.*, **169**, 034531 (2022).
3. C. Grosselindemann et al., *Fuel Cells*, **23**, 442 (2023).
4. M. Riegraf et al., *J. Electrochem. Soc.*, **166**, F865 (2019).
5. A. Nenning, C. Bischof, J. Fleig, M. Bram, and A. K. Opitz, *Energies (Basel)*, **13**, 987 (2020).
6. C. Grosselindemann, N. Russner, S. Dierickx, F. Wankmüller, and A. Weber, *J. Electrochem. Soc.*, **168**, 124506 (2021).
7. A. Hagen, A. K. Padinjarethil, and J. Heijne, *Electrochim. Acta*, **461**, 142672 (2023).
8. V. A. Rojek-Wöckner, A. K. Opitz, M. Brandner, J. Mathé, and M. Bram, *J. Power Sources*, **328**, 65 (2016).
9. (2023), https://geodict.com from Math2Market GmbH GermanyGeoDict software.
10. F. Kullmann, M. Mueller, A. Lindner, S. Dierickx, E. Mueller, and A. Weber, *J. Power Sources*, **587**, 233706 (2023).
11. D. Klotz, A. Weber, and E. Ivers-Tiffée, *Electrochim. Acta*, **227**, 110 (2017).
12. D. G. Goodwin, H. K. Moffat, I. Schoegl, R. L. Speth, and B. W. Weber, (2023), Cantera: An Object-oriented Software Toolkit for Chemical Kinetics, Thermodynamics, and Transport Processes Version 2.5.1.
13. M. Riegraf, K. Develos-Bagarinao, I. Biswas, and R. Costa, *J. Power Sources*, **559**, 232669 (2023).
14. M. Schönleber, D. Klotz, and E. Ivers-Tiffée, *Electrochim. Acta*, **131**, 20 (2014).
15. M. Ouyang et al., *Journal of Energy Chemistry*, **56**, 98 (2021).
16. J. Nielsen, T. Klemenso, and P. Blennow, *J. Power Sources*, **219**, 305 (2012).
17. J. R. Rostrup-Nielsen, *J. Catal.*, **11**, 220 (1968).
18. A. N. Tabish, H. C. Patel, A. Mani, J. Schoonman, and P. V. Aravind, *Electrochim. Acta*, **423**, 140592 (2022).
19. S. Kavurucu Schubert, M. Kusnezoff, A. Michaelis, and S. I. Bredikhin, *J. Power Sources*, **217**, 364 (2012).
20. K. Sasaki et al., *J. Electrochem. Soc.*, **153**, A2023 (2006).
21. M. Riegraf, M. P. Hoerlein, R. Costa, G. Schiller, and K. A. Friedrich, *ACS Catal.*, **7**, 7760 (2017).
22. J. Nielsen, B. R. Sudireddy, A. Hagen, and Å. H. Persson, *J. Electrochem. Soc.*, **163**, F574 (2016).
23. A. Kromp, S. Dierickx, A. Leonide, A. Weber, and E. Ivers-Tiffée, *J. Electrochem. Soc.*, **159**, B597 (2012).
24. A. Hagen, *J. Electrochem. Soc.*, **160**, F111 (2013).
25. A. Weber, *Tech. Mess.*, **88**, 1 (2021).
26. A. Nenning, M. Holzmann, J. Fleig, and A. K. Opitz, *Mater Adv*, **2**, 5422 (2021).

27. J. Bisquert, G. Garcia-Belmonte, F. Fabregat-Santiago, and A. Compte, *Electrochem. Commun.*, **1**, 429 (1999).
28. W. Lai and S. M. Haile, *J. Am. Ceram. Soc.*, **88**, 2979 (2005).
29. S. Dierickx, T. Mundloch, A. Weber, and E. Ivers-Tiffée, *J. Power Sources*, **415**, 69 (2019).
30. V. Sonn, A. Leonide, and E. Ivers-Tiffée, *J. Electrochem. Soc.*, **155**, B675 (2008).
31. J. Nielsen, T. Jacobsen, and M. Wandel, *in Electrochimica Acta*, **56**, 7963 (2011).
32. M. Mogensen, N. M. Sammes, and G. A. Tompsett, *Solid State Ionics*, **129**, 63 (2000).
33. S. Wang, T. Kobayashi, M. Dokiya, and T. Hashimoto, *J. Electrochem. Soc.*, **147**, 3606 (2000).
34. M. A.-F. Öksüzömer, G. Dönmez, V. Saribo ğa, and T. G. Altinçekiç, *Ceram. Int.*, **39**, 7305 (2013).
35. B. C.-H. Steele, *Solid State Ion*, **129**, 95 (2000).
36. S. Wang, H. Inaba, H. Tagawa, and T. Hashimoto, *J. Electrochem. Soc.*, **144**, 4076 (1997).
37. S. R. Bishop, K. L. Duncan, and E. D. Wachsman, *Acta Mater.*, **57**, 3596 (2009).
38. J. Joos, M. Ender, T. Carraro, A. Weber, and E. Ivers-Tiffée, *Electrochim. Acta*, **82**, 268 (2012).
39. P. V. Aravind, J. P. Ouweltjes, and J. Schoonman, *J. Electrochem. Soc.*, **156**, B1417 (2009).
40. I. D. Unachukwu, V. Vibhu, I. C. Vinke, R. A. Eichel, and L. G.-J. (Bert) de Haart, *J. Power Sources*, **556**, 232436 (2023).
41. S. Primdahl and M. Mogensen, *J. Electrochem. Soc.*, **146**, 2827 (1999).
42. D. F. Fairbanks and C. R. Wilke, *Ind. Eng. Chem.*, **42**, 471 (1950).
43. E. L. Cussler, *Diffusion: Mass Transfer in Fluid Systems* (Cambridge University Press, Cambridge) (2009).
44. S. Dierickx, J. Joos, A. Weber, and E. Ivers-Tiffée, *Electrochim. Acta*, **265**, 736 (2018).
45. J. Uecker et al., *Electrochim. Acta*, **452**, 102423 (2023).
46. J. Uecker et al., *ChemElectroChem*, **11**, e202300617 (2024).
47. I. D. Unachukwu et al., *Journal of CO2 Utilization*, **69**, 102423 (2023).
48. A. Leonide, Y. Apel, and E. Ivers-Tiffee, *ECS Trans.*, **19**, 81 (2009).
49. A. Leonide, S. Hansmann, and E. Ivers-Tiffée, *ECS Trans.*, **28**, 341 (2010).
50. E. Ioannidou, M. Chavani, S. G. Neophytides, and D. K. Niakolas, *J. Catal.*, **404**, 174 (2021).
51. A. S. Nielsen, B. A. Peppley, and O. S. Burheim, *Energies (Basel)*, **16**, 987 (2023).
52. R. Einakchi, *thesis*, Université d'Ottawa/University of Ottawa (2016).
53. M. Lortie and R. J. Isaifan, *Journal of Catalysts*, **2015**, 601709 (2015).
54. C. Wheeler, *J. Catal.*, **223**, 191 (2004).
55. N. Guilhaume, D. Bianchi, R. A. Wandawa, W. Yin, and Y. Schuurman, *Catal. Today*, **375**, 282 (2021).